



Density shift of optical lattice clocks via the multiband sampling exact diagonalization method

Yan-Hua Zhou, Xue-Feng Zhang , and Tao Wang *

Department of Physics and Chongqing Key Laboratory for Strongly Coupled Physics, Chongqing University, Chongqing 401331, China
and Center of Modern Physics, Institute for Smart City of Chongqing University in Liyang, Liyang 213300, China



(Received 15 May 2023; accepted 8 August 2023; published 5 September 2023)

Density shift plays an important role in the uncertainty of an optical lattice clock and thus has attracted a great deal of theoretical and experimental studies. However, most of the theoretical research has considered the single-band model and collective approximation, so the density shift of the system at higher temperatures cannot be analyzed accurately. Here we design a numerical algorithm that combines Monte Carlo sampling and exact diagonalization and name it multiband sampling exact diagonalization (MBSED). The MBSED method considers the collision of atoms between multiple bands, so it can provide the density shift of an optical lattice clock with higher precision. Such an algorithm will benefit the numerical simulation of an optical lattice clock and may also be used in other platforms of quantum metrology.

DOI: [10.1103/PhysRevA.108.033304](https://doi.org/10.1103/PhysRevA.108.033304)

I. INTRODUCTION

Time, as one of the fundamental quantities, plays an important role in physics. The precise measurement of time is key to the frontier of research including measurement of fundamental constants [1], detecting gravitational waves [2], testing general relativity [3–5], and searching for dark matter [6,7]. As one of the most accurate time-frequency measurement devices, the optical lattice clock (OLC) platform has made great progress due to experimental efforts in manipulating alkaline-earth or alkaline-earth-like atoms. Recently, the OLC of Bothwell *et al.* has reached an ultrastable level with a fractional frequency measurement uncertainty of 7.6×10^{-21} , so the gravitational redshift at millimeter scale can be resolved [4].

To suppress the quantum projection noise, a large number of atoms need to be prepared in the ground state at each optical lattice site [8]. However, the collisions between atoms can degrade the precision of clocks [9], so the corresponding quantitative calculation becomes vital for quantum metrology. On the other hand, understanding the collisional behavior is also important for both quantum simulations [10–17] and quantum information [18–20] based on the OLC. In the early work in [21], only the *s*-wave scattering was considered due to the inhomogeneous excitation. Then researchers found that the *p*-wave scattering in fact dominates the density shift [22] and proposed the interatomic collisional model, which describes the deep OLC under low axial (*z*) temperature (around 1 μ K). In the calculation, only the lowest axial band was taken into account because the axial energy gap was much larger than the temperature effect. Meanwhile, under the collective approximation, the frequency shift was found to be linear with the atom density; such a prediction was checked by the experiments of Martin *et al.* [23].

In previous work the atoms were assumed to stay at only the lowest band and the density shift was calculated using

approximate methods such as collective or mean-field approximation [22,23]. However, the density shift based on a multiband Hamiltonian and beyond the approximation was not studied. Furthermore, sufficient cooling could not always be guaranteed. Considering the rapid progress of the transportable [24] and space OLC [25], it might be difficult to reach low temperature considering the potentially higher cost of cooling compared with the laboratory. Therefore, it is important to extend the collision model to the multiband case so that the density shift can be estimated with high precision. In this paper we first derive the multiband collisional model of the OLC. Then we develop an advanced algorithm which combines Monte Carlo sampling and exact diagonalization to calculate the density shift of the OLC, which we name multiband sampling exact diagonalization (MBSED). In comparison with the collective approximation, the MBSED method can precisely simulate the density shift in which both the *p* wave and the *s* wave participate. Thus it could present higher accuracy when dealing with a system when the *s*-wave interaction is not effectively suppressed due to excitation inhomogeneity. Furthermore, our *p*-wave interaction is with a different sign than in previous work [22,23]. This is due to the different derivation of the Hamiltonian and it will lead to a huge difference in the *p*-wave scattering length which is fitted through density shift data from the clock measurement. A detailed derivation of our model is given in Appendix A.

The paper is organized as follows. In Sec. II we discuss the effective spin model which further takes into account the axial multiband effect of quantum many-body systems in OLCs. In Sec. III the algorithm of multiband sampling exact diagonalization is discussed. In Sec. IV we simulate a density shift using the MBSED method for both Ramsey and Rabi spectroscopies. Section V provides a summary and an outlook for future work.

II. EFFECTIVE SPIN MODEL

We consider an OLC that uses the $^1S_0(|g\rangle) \leftrightarrow ^3P_0(|e\rangle)$ clock transition in nuclear spin-polarized ^{87}Sr atoms. The

*Corresponding author: tauwang@cqu.edu.cn

atoms are loaded in a deep optical lattice constructed of laser with magic wavelength $\lambda_l = 813.43$ nm [26] so that they experience the same lattice potential. The lattice potential $V_{\text{lat}} = -V_0 \cos^2(k_l z) e^{-2(x^2+y^2)/w_b^2}$, where w_b is the beam waist, which is generally around 45 μm . In the following simulation, we set it as 48 μm . In addition, k_l is the wave number that sets the recoil energy $E_r = \frac{\hbar^2 k_l^2}{2m}$ and V_0 is the lattice depth, which is generally greater than $40E_r$. In this deep lattice regime, atoms are trapped in the center of each lattice site (also with no intersite hopping) and the lattice potential can be approximately treated as a three-dimensional harmonic

trap with potential $V_{\text{ext}} = \frac{1}{2}m\omega_z^2 z^2 + \frac{1}{2}m\omega_r^2(x^2 + y^2)$ where the trap frequency $\nu_r = \sqrt{\frac{V_0}{m}} \frac{2}{\omega_b}$ and $\nu_z = \sqrt{\frac{2V_0}{m}} k_l$. The atom temperature is characterized by the radial temperature T_r and axial temperature T_z , which are fitted by the sideband spectroscopy [21]. When fitting, the theoretical model is based on a harmonic oscillator considering perturbation, so the fitting parameter is not the real temperature, which is why there are two different temperatures in this system. Considering the pairwise interaction between atoms through the s -wave and p -wave channels [10,18,27–30], the single-site Hamiltonian can be written as

$$\begin{aligned} \hat{H}_0 = & \sum_a \int \hat{\psi}_a^\dagger(\mathbf{r}) \left(-\frac{\hbar^2}{2m} \nabla^2 + V_{\text{ext}}(\mathbf{r}) \right) \hat{\psi}_a(\mathbf{r}) d^3\mathbf{r} + \frac{4\pi\hbar^2 a_{eg}^-}{m} \int \hat{\psi}_e^\dagger(\mathbf{r}) \hat{\psi}_e(\mathbf{r}) \hat{\psi}_g^\dagger(\mathbf{r}) \hat{\psi}_g(\mathbf{r}) d^3\mathbf{r} \\ & + \frac{3\pi\hbar^2}{m} \sum_{\alpha,\beta} b_{\alpha\beta}^3 \int \{ [\nabla \hat{\psi}_\alpha^\dagger(\mathbf{r})] \hat{\psi}_\beta^\dagger(\mathbf{r}) - \hat{\psi}_\alpha^\dagger(\mathbf{r}) [\nabla \hat{\psi}_\beta^\dagger(\mathbf{r})] \} \cdot \{ \hat{\psi}_\beta(\mathbf{r}) [\nabla \hat{\psi}_\alpha(\mathbf{r})] - [\nabla \hat{\psi}_\beta(\mathbf{r})] \hat{\psi}_\alpha(\mathbf{r}) \} d^3\mathbf{r} \\ & + \frac{1}{2}\hbar\omega_0 \int [\hat{\rho}_e(\mathbf{r}) - \hat{\rho}_g(\mathbf{r})] d^3\mathbf{r} - \frac{\hbar\Omega_0}{2} \int [\hat{\psi}_e^\dagger(\mathbf{r}) e^{-i(\omega_L t - \mathbf{k} \cdot \mathbf{r})} \hat{\psi}_g(\mathbf{r}) + \text{H.c.}] d^3\mathbf{r}, \end{aligned} \quad (1)$$

where $\hat{\psi}_\alpha(\mathbf{r})$ is a fermionic field operator at position \mathbf{r} for atoms with mass m in the electronic state $\alpha = g$ or e , $\hat{\rho}_\alpha(\mathbf{r}) = \hat{\psi}_\alpha^\dagger(\mathbf{r}) \hat{\psi}_\alpha(\mathbf{r})$ is the corresponding density operator, and a_{eg}^- is the scattering length describing collisions between two atoms in the antisymmetric electronic state $\frac{1}{\sqrt{2}}(|ge\rangle - |eg\rangle)$. The p -wave scattering volumes b_{gg}^3 , b_{ee}^3 , and b_{eg}^3 represent three possible electronic symmetric states $|gg\rangle$, $|ee\rangle$, and $\frac{1}{\sqrt{2}}(|eg\rangle + |ge\rangle)$, respectively. In addition, ω_L is the frequency of the probing laser and \mathbf{k} is its wave vector; $\mathbf{k} = \{k_x, 0, k_z\} \approx \{k_p \Delta\theta, 0, k_p\}$, where $\Delta\theta$ is a small misalignment angle between the probing laser and the lattice laser; ω_0 is the atomic transition frequency and Ω_0 is the bare Rabi frequency. The previous works in [22,23] focused on the system at low temperature (around 1 μK), so only the lowest axial band needs to be considered. In contrast, as shown in Fig. 1(a), the distribution of higher axial bands cannot be ignored in a high-temperature system. Therefore, different from previous studies [22], the expansion of the field operators in a noninteracting harmonic eigenbasis is not limited to the lowest axial band

$$\hat{\psi}_\alpha(\mathbf{r}) = \sum_{\vec{n}} \hat{c}_{\alpha\vec{n}} \phi_{n_x}(x) \phi_{n_y}(y) \phi_{n_z}(z), \quad (2)$$

where $\hat{c}_{\alpha\vec{n}}$ annihilates a fermion in the motional mode $\vec{n} = \{n_x, n_y, n_z\}$ and electronic state α . Because all trap frequencies are much greater than the characteristic interaction energy, the motional degrees of freedom are effectively frozen [22]. Considering the energy conservation law and anharmonicity of the trap, the external states of atoms could remain the same or be exchanged only after the collision. Then the atom distribution in the external states is fixed and obtained by sampling as the Boltzmann distribution, so the effective model can be greatly simplified [22]. After mapping into a spin- $\frac{1}{2}$ model with $|g\rangle \rightarrow |\downarrow\rangle$ and $|e\rangle \rightarrow |\uparrow\rangle$, the many-body

interacting Hamiltonian can be written as

$$\begin{aligned} \frac{\hat{H}_s}{\hbar} = & -2\pi\delta \sum_i \hat{S}_i^z - 2\pi \sum_i \Omega_i \hat{S}_i^x - \sum_{i \neq j} C_{i,j} \frac{\hat{S}_i^z + \hat{S}_j^z}{2} \\ & - \sum_{i \neq j} X_{i,j} \hat{S}_i^z \hat{S}_j^z - \sum_{i \neq j} J_{i,j} \hat{S}_i \cdot \hat{S}_j, \end{aligned} \quad (3)$$

where \hat{S}_i^γ ($\gamma = x, y, z$) denotes the spin operator for the i th external state, $\delta = (\omega_L - \omega_0)/2\pi$ is the laser detuning from atomic resonance, and Ω_i is the mode-dependent Rabi

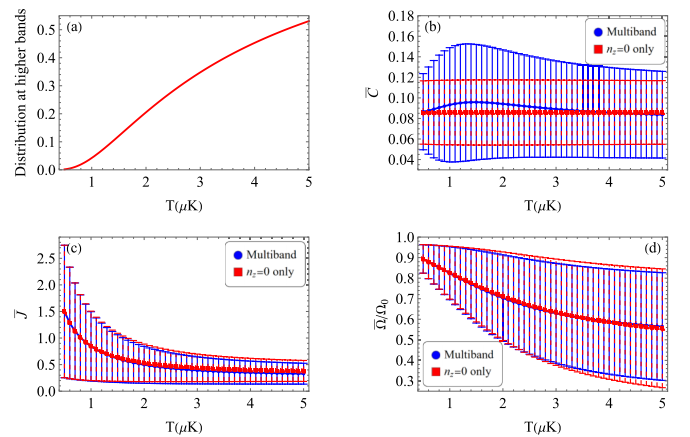


FIG. 1. Several quantities as a function of system temperature $T_r = T_z = T$ with lattice frequency $\nu_z = 66\,000$ Hz and $\nu_r = 250$ Hz. (a) Thermal populated distribution for atoms at higher bands ($n_z > 0$). The thermally averaged values of collision parameters (b) $C_{i,j}$ and (c) $J_{i,j}$ are shown along with their corresponding standard deviations. (d) Thermally averaged value and standard deviation of the normalized Rabi frequency Ω_i/Ω_0 with the misalignment angle $\Delta\theta = 10$ mrad.

frequency (see Appendix A). The coefficients of the effective spin interactions are explicitly expressed as

$$\begin{aligned} J_{i,j} &= a_{eg}^- G_{i,j}^S + b_{eg}^3 G_{i,j}^P, \\ C_{i,j} &= (b_{ee}^3 - b_{gg}^3) G_{i,j}^P, \\ X_{i,j} &= (b_{ee}^3 - 2b_{eg}^3 + b_{gg}^3) G_{i,j}^P, \end{aligned} \quad (4)$$

where $G_{i,j}^S$ and $G_{i,j}^P$ denote the interaction strengths arising from the s wave and p wave, respectively. One way to solve the time evolution of the Hamiltonian (3) and calculate the density shift is using the collective approximation [23], which takes the thermal average of all the coefficients to replace mode-dependent ones. In this approximation, the total spin is confined in the Dicke space with total spin $S = N/2$ (see Appendix B for more information about the collective approximation). This method is applicable when the system is in a collective regime where the standard deviation of those coefficients are small. To see the standard deviation of mode-dependent coefficients, we sample the external states for atoms according to the Boltzmann distribution and plot the thermally averaged value of $C_{i,j}$, $J_{i,j}$, and Ω_i/Ω_0 and their corresponding standard deviations as a function of system temperature $T_r = T_z = T$. The result is shown in Fig. 1. The statistic property of $X_{i,j}$ is not shown in Fig. 1 because it is proportional to $C_{i,j}$ [see Eq. (4)].

As we can see in Fig. 1(d), the standard deviation of the normalized Rabi frequency Ω_i/Ω_0 increases significantly with the system temperature, which will induce strong excitation inhomogeneity and break the collective property of the OLC system. The collective approximation may fail when describing such a system. Therefore, in order to study the density shift beyond the collective regime, we have developed a numerical algorithm called multiband sampling exact diagonalization, which is introduced in the next section.

Furthermore, as shown in Fig. 1(b), when the system temperature is around 1.5 μ K, atoms staying in the excited axial state will have a non-negligible effect on the thermally averaged value of $C_{i,j}$ (which increases about 12% compared with the case that considers only the lowest band). In addition, after considering the multiband distribution of the axial external state, we find that the standard deviation of $C_{i,j}$ increases. Because the density shift is mainly caused by the p -wave interaction which is characterized by $C_{i,j}$, it is necessary to consider the multiband model in an optical lattice clock system.

III. MBSED METHOD

The algorithm of the MBSED method is pretty straightforward; the flow chart diagram is shown in Fig. 2(a). The main process can be concisely described as follows. (i) A number of samples are obtained according to the Boltzmann distribution. (ii) Because the number of particles in each site is not too high, the time evolution of the quantum state can be calculated via diagonalization of the Hamiltonian (3). (iii) As shown in Fig. 2(b), the probability of the excited state (the spectrum) can be estimated by taking the mean value of all the samples.

We first use the Monte Carlo method to generate samples that follow the Boltzmann distribution. The corresponding

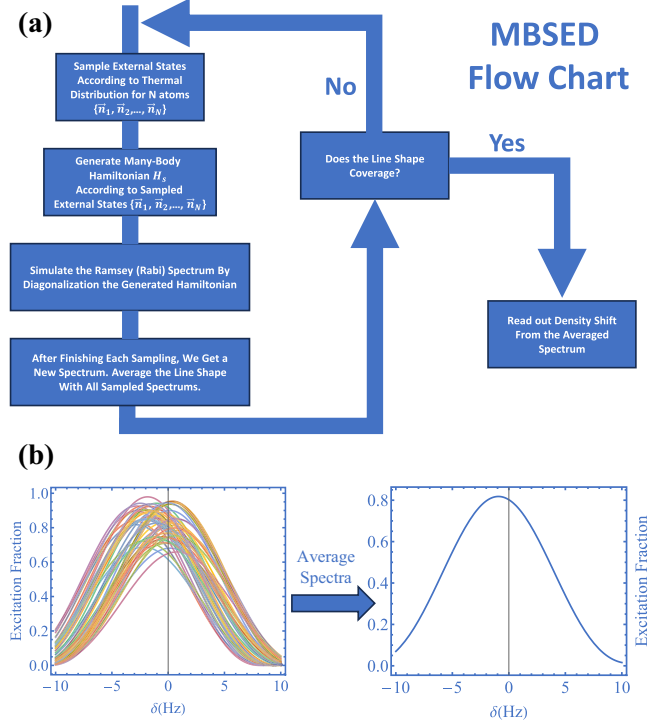


FIG. 2. (a) Flow chart of the MBSED algorithm. After each sampling, we diagonalize the many-body Hamiltonian according to sampled external states and simulate the excitation spectrum (Ramsey or Rabi). Then we average the spectrum line shape with all previously sampled results. After many samplings, the excitation spectrum can be precisely obtained as well as the density shift. (b) Schematic plot for the average spectrum. In the left plot, each line shape is simulated by Monte Carlo sampled external states. The right plot is the thermally averaged spectrum and the density shift is read out from it.

partition function can be represented as

$$Z = \sum_{n_z, n_r} (n_r + 1) \exp \left(-\frac{\hbar\omega_z(n_z + \frac{1}{2})}{k_B T_z} - \frac{\hbar\omega_r(n_r + 1)}{k_B T_r} \right), \quad (5)$$

in which ω_z (ω_r) is the axial (radial) trap frequency, T_z (T_r) is the axial (radial) temperature, and $n_r = n_x + n_y$ labels the radial motional state with degeneracy $n_r + 1$. The number of eigenstates N_z (N_r) in the axial (radial) direction can be estimated with $U_r/\hbar\omega_z$ ($U_r/\hbar\omega_r$), where U_r is the depth of the lattice potential energy. Typically, N_z is approximately equal to 5 and N_r is approximately equal to 1000. Then the motional states of all the atoms are sampled according to the distribution (5). Notice that, because of the degeneracy in the radial direction, the index (n_x, n_y) should be randomly selected after fixing (n_z, n_r) . Meanwhile, the samples with atoms located in the same motional state (n_x, n_y, n_z) have to be kicked out due to the Pauli exclusion principle. Such processes are extremely rare at high temperature and less than one per 1000 at 1 μ K, so its influence can be omitted.

After the motional index \vec{n} is sampled, the corresponding coefficients of the Hamiltonian (3) on the basis of harmonic eigenstates can be directly calculated (see Appendix A for details). Then all the eigenstates $|\psi\rangle_m$ with eigenenergy E_m

can be obtained by using the exact diagonalization. Assuming the system is prepared in the initial state $|\psi\rangle_0$, i.e., the ground state $|\psi\rangle_G = |\downarrow\downarrow\cdots\downarrow\rangle$, the time-dependent wave function turns out to be

$$|\psi(t)\rangle = \sum_m e^{-iE_m t/\hbar} \langle\psi|\psi\rangle_0 |\psi\rangle_m. \quad (6)$$

However, the full diagonalization requires the atom number N to be less than approximately 20, so it is better to find a way to truncate the Hilbert space. The initial state $|\psi\rangle_G$ stays at the subspace with total spin $S = \frac{N}{2}$ but evolves into other subspaces due to the interaction and inhomogeneous excitations. The good thing is that the variation of $\langle S \rangle$ is very slow, so we can project the Hamiltonian to the subspaces with total spin equal to $\{\frac{N}{2}, \frac{N}{2} - 1, \dots, \frac{N}{2} - m\}$ when the evolution time is not so long. The selection of the truncation number m depends on parameters of the OLC such as temperatures and misalignment angle.

The physical observables can be numerically calculated by taking the mean value of all the samples, such as the probability of the excited state. If the deviation of the mean value converges to a certain precision, we output the final result; otherwise, the sampling will continue.

IV. NUMERICAL SIMULATION

The MBSED method is very useful to numerically simulate the spectroscopy with high precision in an OLC beyond the collective regime. To demonstrate its efficiency, the densities of both Ramsey spectroscopy and Rabi spectroscopy are estimated. First, the values of scattering lengths b_{ee} and b_{eg} should be fitted using the MBSED method. Based on the experimental data from Martin *et al.* [23], the fitted scattering lengths are $b_{ee} = 150.19a_B$ and $b_{eg} = 192.34a_B$ (a_B is the Bohr radius). More details related to the fitting process are shown in Appendix C. Note that the scattering lengths we obtained are greatly different from those in Ref. [14] (different sign), which we think may result from the different derivation of the effective model. Therefore, we include the derivation in detail in Appendix A, although it has no effect on our conclusion. Note that all simulations are based on the Hamiltonian (3), in which inelastic collisions are neglected. Therefore, our focus is solely on the short-time evolution, allowing us to disregard decoherence resulting from the inelastic processes.

A. Density shift in Ramsey spectroscopy

Ramsey spectroscopy has become a well-developed tool in time measurement [4,31]. Compared to Rabi spectroscopy, Ramsey spectroscopy can obtain narrower spectrum lines in a shorter light-atom interaction time.

In the Ramsey process, the atoms are initially prepared in the ground state. A probing pulse with detuning δ is added during the pulse time t_1 . Then the atoms freely evolve for a dark time τ (without a probing laser). Finally, a probing laser with the same detuning will be used for duration t_2 . Usually, the Rabi frequency is much greater than the interaction strength in an experimental setup. Thus, the influence of interatomic collisions can only be taken into account in the

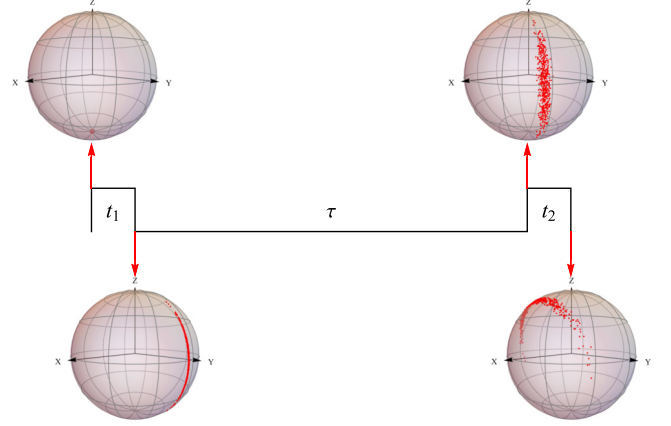


FIG. 3. Schematic diagram for the Ramsey spectroscopy process of an ensemble of atoms. Here each dot represents the quantum state of one atom on the Bloch sphere.

dark time. Figure 3 shows a Ramsey process of an ensemble of atoms in the presentation of the Bloch sphere.

As demonstrated in Fig. 4, the peak of the excitation fraction in Ramsey spectroscopy is located at zero detuning if the atomic collision is not considered. However, in the real experiment, the collision can result in the deviation of the peak $\delta = 2\pi\Delta\nu$, which is equal to the density shift. Under the collective approximation, the density shift $2\pi\Delta\nu \approx (N-1)(\bar{X} \cos 2\pi\bar{\Omega}t_1 - \bar{C})$ (see Appendix D). In Ramsey spectroscopy, the detuning and collision in pulse time can be ignored; therefore, the excitation fraction at the end of the first pulse $p_1 = \frac{1}{2} - \frac{1}{2}\cos 2\pi\bar{\Omega}t_1$. Thus, the density shift under the collective approximation could be expressed as $2\pi\Delta\nu \approx (N-1)[\bar{X}(1-2p_1) - \bar{C}]$, which is linear with p_1 .

To study the density shift beyond the collective regime, we use the MBSED method. During the MBSED simulation, the time evolution of the pulse time can be greatly simplified. Because the interaction is negligible in comparison with the remaining terms, each atom in the motional state is governed by a local 2×2 matrix. On the other hand, during the dark time, there is no atom-light interaction. Therefore,

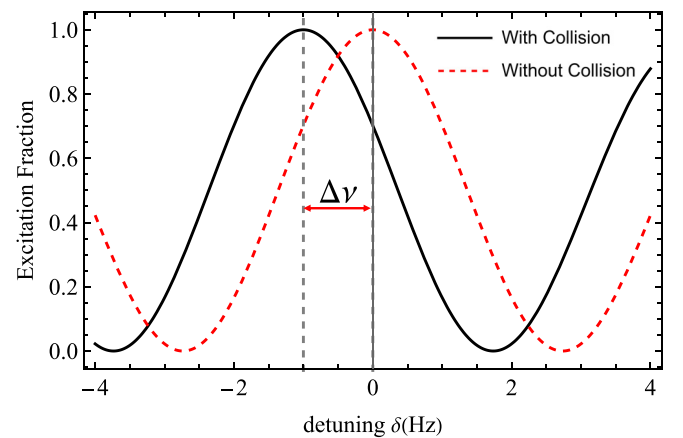


FIG. 4. Schematic Ramsey spectrum with and without atomic collision.

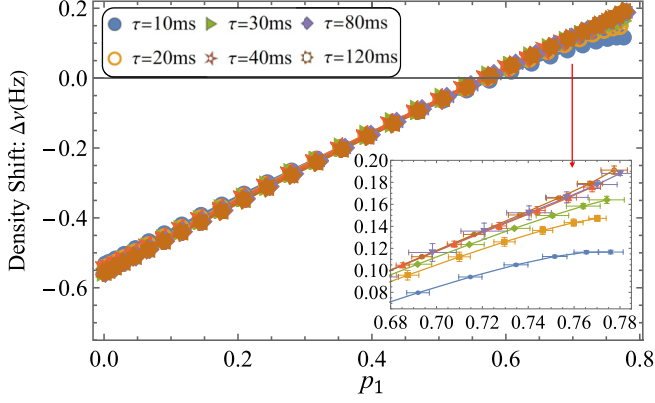


FIG. 5. Density shifts of Ramsey spectroscopy at different dark time durations τ . The x axis plots the excitation fraction at the end of the first pulse. The temperature is set to $T_z = T_r = 3 \mu\text{K}$ and the atom number is 5. The inset shows the smaller scale.

the Hamiltonian keeps the $U(1)$ symmetry with conserved quantities $M^z = \sum_i \hat{S}_i^z$ and thus could be block diagonalized. In addition, the detuning δ will not change the eigenvector V of the dark time Hamiltonian and only changes the eigenvalue with a detuning-related term $\hbar\delta M^z$. Considering the Ramsey spectroscopy is obtained by changing the detuning, the diagonalization can be performed just once. In the following simulation, we set $\nu_z = 66 \text{ kHz}$ and $\nu_r = 250 \text{ Hz}$ and we set the misaligned angle between the lattice and probing laser $\Delta\theta = 10 \text{ mrad}$ to make sure that there will be a strong noncollective effect during the time evolution. The bare Rabi frequency Ω_0 is set to 500 Hz and has less effect on the density shift since it is much higher than the collision coefficients. In order to figure out the relation between the density shift and p_1 , we vary p_1 by tuning t_1 at fixed $t_2 = \frac{1}{4\Omega}$ (the second pulse is a $\pi/2$ pulse). First, the role played by the dark time is checked. Under the collective approximation, the density shift satisfies $2\pi\Delta\nu \approx (N-1)(\bar{X}\cos 2\pi\Omega t_1 - \bar{C})$ while $|\bar{X}\tau| \ll 1$. During our simulation, \bar{X} is around $2\pi \times 0.05$. If $\tau = 120 \text{ ms}$, then $|\bar{X}\tau| = 0.0377 \ll 1$. Therefore, according to the collective approximation, the density shift should be very insensitive to τ when $\tau < 120 \text{ ms}$. However, as shown in Fig. 5, through the MBSED method we find that even when $|\bar{X}\tau| \ll 1$ the density shift is obviously affected by τ for a noncollective system, especially when the dark time is short.

Then, as mentioned before, the temperature can result in the invalidity of the collective approximation, so it is worth verifying it. In Fig. 6 we compare the results of both the collective approximation and MBSED methods at different temperatures. It is obvious that there is a large deviation between them when $T_z = T_r > 3 \mu\text{K}$. From Fig. 6 we can extract the excitation fraction P_0 where the corresponding density shift equals zero. The collective approximation gives the temperature-independent value $P_0 = 0.643$. In contrast, as shown in Fig. 7, the simulation from the MBSED method shows that P_0 decreases while temperature increases. Therefore, the MBSED method can remedy the drawback of the collective approximation and gives a more precise prediction of the density shift beyond the collective regime. In addition, the MBSED result that considers only the lowest band is also

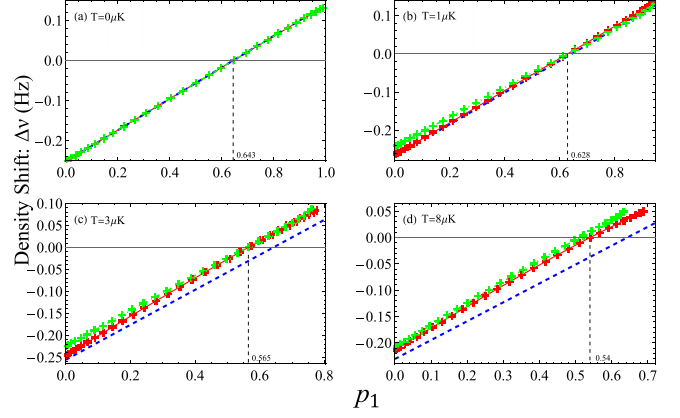


FIG. 6. Comparison of the density shift between numerical simulation with multiple bands (red solid line), collective approximation with multiple bands (blue dashed line), and numerical simulation with only the lowest band (green dot-dashed line) at different temperatures with the atom number equal to 5: (a) $T_z = T_r = 0 \mu\text{K}$, (b) $T_z = T_r = 1 \mu\text{K}$, (c) $T_z = T_r = 3 \mu\text{K}$, and (d) $T_z = T_r = 8 \mu\text{K}$. The x axis plots the excitation fraction at the end of the first pulse. The vertical dashed lines mark the excitation fraction with a zero-density shift.

shown in Fig. 6. We could see that the value of the density shift under the lowest-band approximation is different from that of the multiband case even at $T = 1 \mu\text{K}$; therefore, it is necessary to study the density shift under the multiband model when the excited band distribution is non-negligible. Next we want to check the linear relation between the density shift and atom number predicted by the collective approximation, because this relation is usually used to estimate the density shift in the experiment [22]. Meanwhile, we also use this relation to fit the system parameters (see Appendix C). In Fig. 8, after being divided by $N-1$, the curves of the density shift of different atom numbers almost overlap with each other, so the excitation fraction with a zero-density shift is almost unchanged with atom number. To be more explicit, we performed a linear fit of the density shift at excitation fraction $P_e = 0.2$ for different atom numbers. As shown in the legend of Fig. 8, the linearity of the relation is very good. Considering the corresponding temperature is $T_r = T_z = 3 \mu\text{K}$, this means

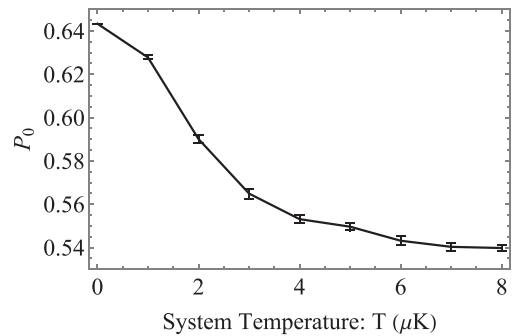


FIG. 7. Excitation fraction for zero-density shift at different temperatures. The system parameters are the same as in Fig. 6.

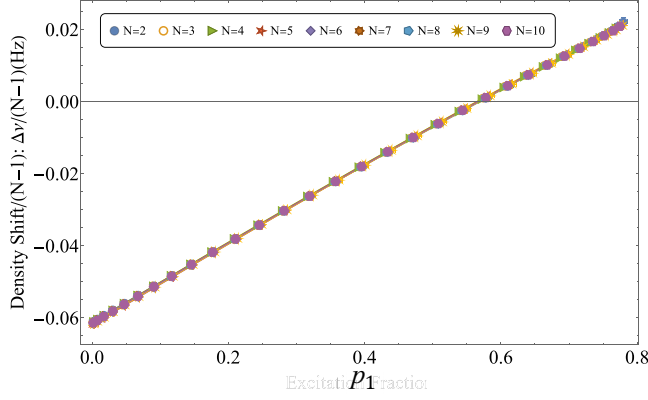


FIG. 8. Rescaled density shift in Ramsey spectroscopy with different numbers of atoms. The x axis plots the excitation fraction at the end of the first pulse. The temperature is set to $T_z = T_r = 3 \mu\text{K}$.

the linear relation of the density shift to atom number in Ramsey spectroscopy remains for high temperature.

Finally, because OLCs work at a wide range of lattice depths, it is important to know how the density shift changes with the lattice depth. In the collective regime, the p -wave interaction dominates the density shift and the p -wave interaction parameters $C_{i,j}$ and $X_{i,j}$ are proportional to $V_0^{5/4}$. Therefore, the density shift should be proportional to $V_0^{5/4}$ under the collective regime. To see the density shift scaling of V_0 beyond the collective regime, the density shift is simulated using the MBSED method with $t_1 = t_2$ as a $\frac{\pi}{2}$ pulse at different lattice depths (from $50E_r$ to $150E_r$), different external state distributions, and different misalignment angles $\Delta\theta$. The external state distribution is characterized by β , which has the dimension of temperature (μK). The relationship between the system temperature and β is defined as $T = \sqrt{\frac{V_0}{100E_r}} \beta$ and the data are fitted with the function of the form aV_0^n (a and n are fitted parameters) at each β and $\Delta\theta$. The result is shown in Fig. 9. We could see that the fitted parameter n decreases as

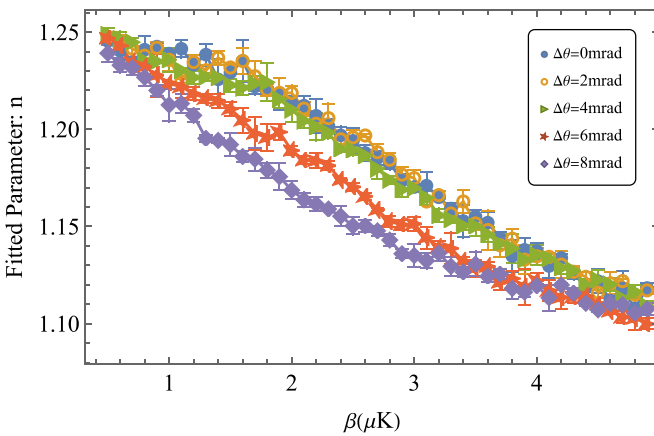


FIG. 9. Fitted parameter n of the function aV_0^n for different β at different misalignment angles $\Delta\theta$. The system temperature $T = \sqrt{\frac{V_0}{100E_r}} \beta$.

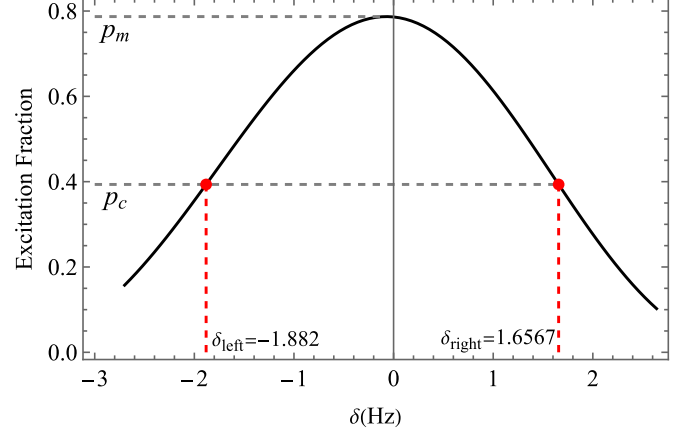


FIG. 10. Schematic plot for the simulation density shift of Rabi spectroscopy using the MBSED method. Here p_m is the maximum excitation fraction of a π pulse Rabi spectrum and $p_c = \frac{p_m}{2}$ is the half-excitation fraction; δ_{left} and δ_{right} are the corresponding negative detuning and positive detuning of two half-excitation fraction points.

β increases. For systems with large $\Delta\theta$, the decrease is even greater.

B. Density shift in Rabi spectroscopy

In Rabi spectroscopy, the atoms are also initially prepared in the ground state and then excited by applying a probe laser with detuning δ with duration time t . During our simulation, we set the duration of probing time t as a π pulse. During the experiment, the clock transition frequency is obtained by the average of two frequencies with the same certain excitation fraction p_c . To reach a maximum sensitivity, p_c is generally chosen as half of the maximum excitation fraction p_m of the Rabi spectrum. The density shift is determined as $\Delta\nu = \frac{\delta_{\text{left}} + \delta_{\text{right}}}{2}$, where δ_{left} and δ_{right} are the negative detuning and positive detuning of two half-excitation points. A schematic plot is shown in Fig. 10.

First, the relation between the density shift and Rabi frequency is checked. From Fig. 11 we can find that the density heavily depends on the magnitude of the Rabi frequency while

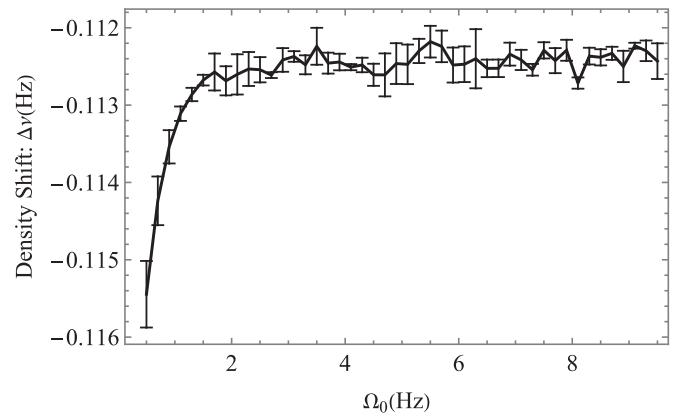


FIG. 11. Density shift of Rabi spectroscopy at different Rabi frequencies. The temperature is set to $T_z = T_r = 3 \mu\text{K}$ and the atom number is 5.

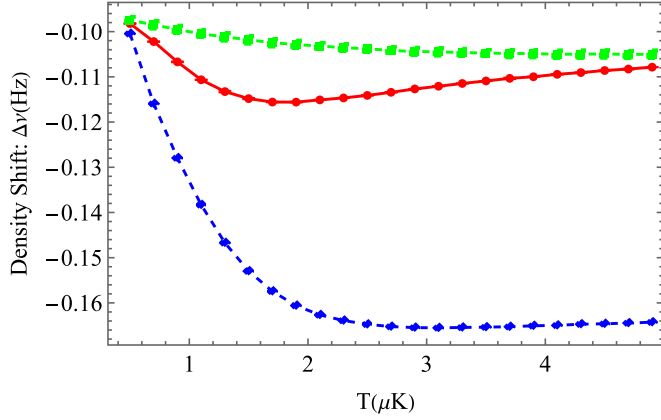


FIG. 12. Comparison of the density shift between numerical simulation based on the multiband model (red solid line), the lowest-band model (green dot-dashed line), and collective approximation (blue dashed line) at different temperatures with the atom number equal to 5.

the system is in a strongly correlated regime. In this regime, the Rabi frequency is no longer a magnitude larger than the interatomic collision energy scale, which is around 0.06 Hz, and the atomic scattering will tend to dominate the many-body dynamics and strongly distort the Rabi spectrum, which is bad for clock operation. Thus, we set the bare Rabi frequency to $\Omega_0 = 5$ Hz, which is much greater than atomic interaction energy scale in the following discussion.

Then we want to study the influence of temperature. The collective approximation can also be used in Rabi spectroscopy, but the time evolution cannot be solved analytically. Therefore, we numerically calculated the density shift under the collective approximation and compared it with that obtained using the MBSED method. Figure 12 shows the density shift of both methods at different temperatures. As in the Ramsey case, it indicates that the collective approximation is suitable only for low temperatures. At higher temperatures, it will overestimate the density shift.

Next we check if the density shift has a linear relation with the atom number. From Fig. 13 we can find that the density shift is still linear with $N - 1$ in a noncollective

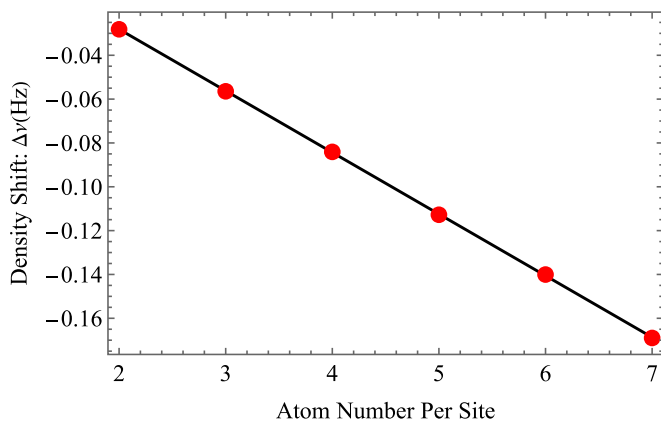


FIG. 13. Density shift in Rabi spectroscopy with different numbers of atoms in a noncollective regime. The temperature is set to $T_z = T_r = 3$ μ K and the misalignment angle $\Delta\theta = 10$ mrad.

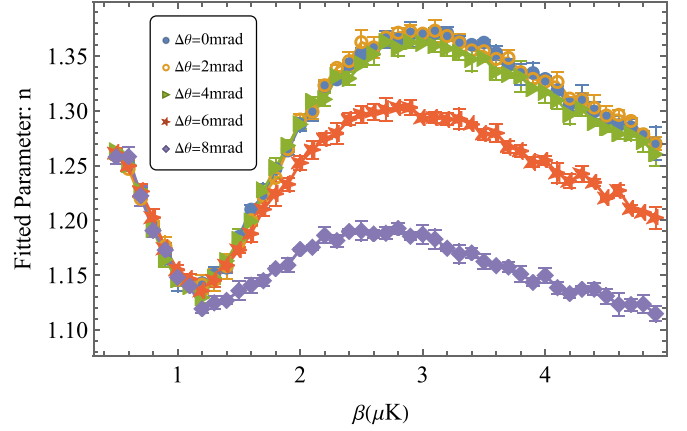


FIG. 14. Fitted parameter n of the function aV_0^n for different β at different misalignment angles $\Delta\theta$. The system temperature $T = \sqrt{\frac{V_0/E_r}{100}} \beta$.

system, where N is the atom number. Finally, we simulate the density shift of Rabi spectroscopy at different lattice depths. Similar to the Ramsey case, we first simulate the density shift under different lattice depths V_0 (also from $50E_r$ to $150E_r$), distributions β , and misalignment angles $\Delta\theta$. The relationship between β and the system temperature T is defined as $T = \sqrt{\frac{V_0}{100E_r}} \beta$. The data are fitted with aV_0^n at each β and $\Delta\theta$. The probing time t is set as a π pulse. The result is shown in Fig. 14. We could see that the density shift is still proportional to $V_0^{5/4}$ when the system is in a low-temperature regime ($\beta \approx 0.5$ μ K). However, the fitted parameter n increases to around 1.4 when $\beta \approx 3$ μ K for a small misalignment system ($\Delta\theta < 5$ mrad).

V. CONCLUSION AND OUTLOOK

In this paper we extended the effective spin Hamiltonian which describes the atomic collisions of the OLC from the single-band case to the multiband case so that the OLC system at higher temperatures can be described. To deal with the extended Hamiltonian, we developed a numerical algorithm, MBSED, which combines the Monte Carlo method to sample the distribution of atoms and exact diagonalization to simulate the time evolution of the OLC system. After implementing the MBSED method on both Ramsey and Rabi spectroscopies, we found that the collective approximation method is valid only for the system at low temperatures. For both Ramsey and Rabi spectroscopies, we found that the linear relation between the density shift and atom number still holds and in the Ramsey spectrum the special excitation fraction where the density shift equals zero decreases with increasing temperature.

The quantum many-spin model has been extensively studied in the field of condensed-matter physics. In order to solve such quantum many-body problems, numerous numerical algorithms have been developed, including exact diagonalization, quantum Monte Carlo, and matrix product states. However, in the field of OLCs, there is no work that adopts these algorithms to solve the quantum many-body Hamiltonian. Thus, our work provides a bridge between OLCs

and quantum many-body computation. Many issues could be investigated in future work. One direction would be checking how average entanglement entropy grows with the atom number to determine whether the model could deal with the matrix product state. Another direction could be further consideration of the inelastic collision between atoms, which was disregarded in this paper.

ACKNOWLEDGMENTS

We wish to thank A. M. Rey for discussions. This work was supported by the National Science Foundation of China under Grant No. 12274045. X.-F.Z. acknowledges funding from the National Science Foundation of China under Grants No. 12274046, No. 11874094, and No. 12147102 and Fundamental Research Funds for the Central Universities Grant No. 2021CDJZYJH-003. T.W. acknowledges funding from the Program of State Key Laboratory of Quantum Optics and Quantum Optics Devices (Grant No. KF202211).

APPENDIX A: EFFECTIVE HAMILTONIAN

The Hamiltonian (1) can be divided into four parts, that is, $\hat{H}_0 = \hat{H}_0^{\text{ext}} + \hat{H}_0^s + \hat{H}_0^p + \hat{H}_0^{\text{Rabi}}$:

$$\begin{aligned}\hat{H}_0^{\text{ext}} &= \sum_{\alpha} \int \hat{\psi}_{\alpha}^{\dagger}(\mathbf{r}) \left(-\frac{\hbar^2}{2m} \nabla^2 + V_{\text{ext}}(\mathbf{r}) \right) \hat{\psi}_{\alpha}(\mathbf{r}) d^3\mathbf{r}, \\ \hat{H}_0^s &= \frac{4\pi\hbar^2 a_{eg}^-}{m} \int \hat{\psi}_e^{\dagger}(\mathbf{r}) \hat{\psi}_e(\mathbf{r}) \hat{\psi}_g^{\dagger}(\mathbf{r}) \hat{\psi}_g(\mathbf{r}) d^3\mathbf{r}, \\ \hat{H}_0^p &= \frac{3\pi\hbar^2}{m} \sum_{\alpha,\beta} b_{\alpha\beta}^3 \int \{ [\nabla \hat{\psi}_{\alpha}^{\dagger}(\mathbf{r})] \hat{\psi}_{\beta}^{\dagger}(\mathbf{r}) - \hat{\psi}_{\alpha}^{\dagger}(\mathbf{r}) [\nabla \hat{\psi}_{\beta}^{\dagger}(\mathbf{r})] \} \\ &\quad \cdot \{ [\nabla \hat{\psi}_{\alpha}(\mathbf{r})] \hat{\psi}_{\beta}(\mathbf{r}) - \hat{\psi}_{\alpha}(\mathbf{r}) [\nabla \hat{\psi}_{\beta}(\mathbf{r})] \} d^3\mathbf{r}, \\ \hat{H}_0^{\text{Rabi}} &= \frac{1}{2} \hbar \omega_0 \int [\hat{\rho}_e(\mathbf{r}) - \hat{\rho}_g(\mathbf{r})] d^3\mathbf{r} \\ &\quad - \hbar \pi \Omega_0 \int [\hat{\psi}_e^{\dagger}(\mathbf{r}) e^{-i(\omega_L t - \mathbf{k} \cdot \mathbf{r})} \hat{\psi}_g(\mathbf{r})] \\ &\quad - \hbar \pi \Omega_0 \int [\hat{\psi}_g^{\dagger}(\mathbf{r}) e^{i(\omega_L t - \mathbf{k} \cdot \mathbf{r})} \hat{\psi}_e(\mathbf{r})].\end{aligned}$$

Let us first deal with \hat{H}_0^{ext} . Under typical working conditions, the external potential can be approximately treated as a harmonic trap $V_{\text{ext}}(\mathbf{r}) = \frac{1}{2} m \omega_z z^2 + \frac{1}{2} m \omega_r (x^2 + y^2)$. By expanding the field operator using (2), we have

$$\hat{H}_0^{\text{ext}} = \sum_{\alpha} \sum_{\vec{n}} \left[\hbar \omega_z \left(n_z + \frac{1}{2} \right) + \hbar \omega_r (n_x + n_y + 1) \right] \hat{c}_{\alpha, \vec{n}}^{\dagger} \hat{c}_{\alpha, \vec{n}}.$$

Therefore, \hat{H}_0^{ext} offers only a constant energy shift.

Now let us turn to \hat{H}_0^s . As before, we expand the field operator under the harmonic basis

$$\begin{aligned}\hat{H}_0^s &= \frac{4\pi\hbar^2 a_{eg}^-}{m} \sum_{\vec{n}_1, \vec{n}_2, \vec{n}_3, \vec{n}_4} \hat{c}_{e, \vec{n}_1}^{\dagger} \hat{c}_{g, \vec{n}_2}^{\dagger} \hat{c}_{g, \vec{n}_3} \hat{c}_{e, \vec{n}_4} \int \phi_{n_{x1}} \phi_{n_{x2}} \phi_{n_{x3}} \phi_{n_{x4}} dx \\ &\quad \times \int \phi_{n_{y1}} \phi_{n_{y2}} \phi_{n_{y3}} \phi_{n_{y4}} dy \int \phi_{n_{z1}} \phi_{n_{z2}} \phi_{n_{z3}} \phi_{n_{z4}} dz.\end{aligned}$$

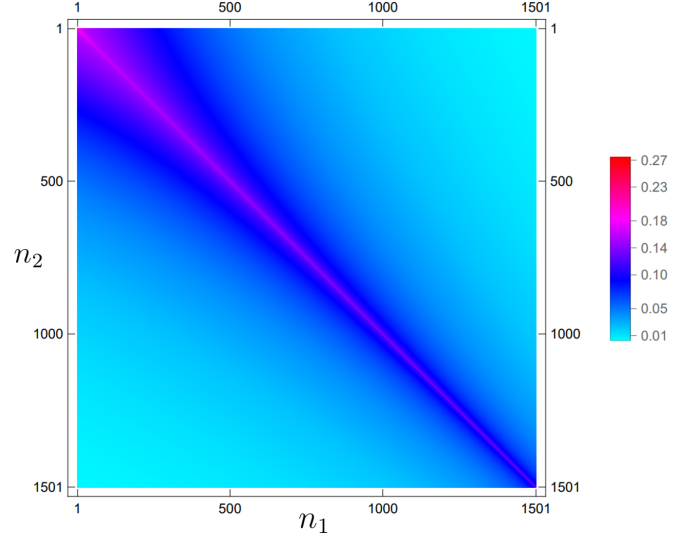


FIG. 15. Mode dependence of $s(n_1, n_2, n_1, n_2)$.

By defining $\xi_{\gamma} = \sqrt{\frac{m\omega_{\gamma}}{\hbar}} \gamma = R_{\gamma} \gamma$ ($\gamma = x, y, z$) and

$$s(n_1, n_2, n_3, n_4) = \int \frac{H_{n_1}(\xi) H_{n_2}(\xi) H_{n_3}(\xi) H_{n_4}(\xi)}{\pi \sqrt{2^{n_1+n_2+n_3+n_4} n_1! n_2! n_3! n_4!}} e^{-2\xi^2} d\xi,$$

where $H_n(\xi)$ are Hermite polynomials, we could simplify \hat{H}_0^s as

$$\begin{aligned}\hat{H}_0^s &= \frac{4\pi\hbar^2}{m} a_{eg}^- R_r^2 R_z \sum_{\vec{n}_1, \vec{n}_2, \vec{n}_3, \vec{n}_4} \hat{c}_{e, \vec{n}_1}^{\dagger} \hat{c}_{g, \vec{n}_2}^{\dagger} \hat{c}_{g, \vec{n}_3} \hat{c}_{e, \vec{n}_4} \\ &\quad \times s(n_{x1}, n_{x2}, n_{x3}, n_{x4}) s(n_{y1}, n_{y2}, n_{y3}, n_{y4}) \\ &\quad \times s(n_{z1}, n_{z2}, n_{z3}, n_{z4}).\end{aligned}$$

Because the motional degrees of freedom are effectively frozen due to the energy conservation constraint [22], the motional quanta can remain the same or be fully exchanged

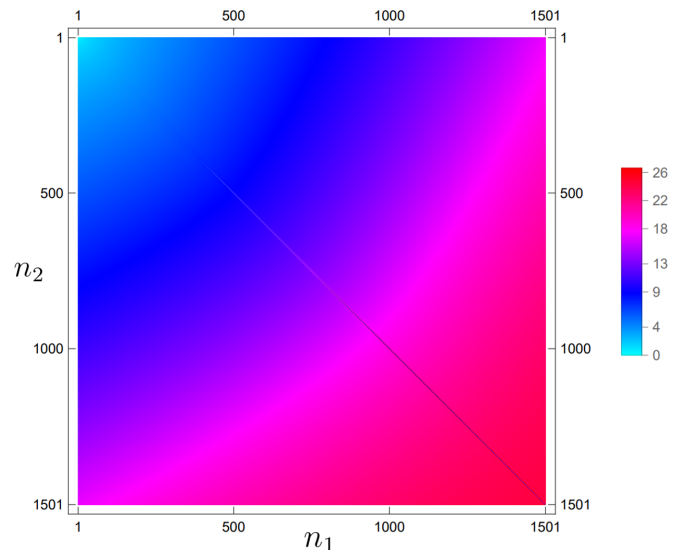


FIG. 16. Mode dependence of $p(n_1, n_2, n_1, n_2)$.

only after collision. Therefore, only terms satisfying one of the equations

$$\{\vec{n}_3, \vec{n}_4\} = \{\vec{n}_2, \vec{n}_1\}, \quad \{\vec{n}_3, \vec{n}_4\} = \{\vec{n}_1, \vec{n}_2\} \quad (\text{A1})$$

are relevant in our calculation. The parameter space of $s(i, j, k, l)$ could be squeezed to a two-dimensional space

from a four-dimensional space. In Fig. 15 we show the mode dependence of $s(n_1, n_2, n_1, n_2)$.

Next we define

$$S_{\vec{n}_i, \vec{n}_j} = s(n_{x_i}, n_{x_j}, n_{x_j}, n_{x_i})s(n_{y_i}, n_{y_j}, n_{y_j}, n_{y_i})(n_{z_i}, n_{z_j}, n_{z_j}, n_{z_i}).$$

Then

$$\begin{aligned} \hat{H}_0^s &= \frac{2\pi\hbar}{m} R_r^2 R_z a_{eg}^- \sum_{\vec{n}_1 \neq \vec{n}_2} S_{\vec{n}_1, \vec{n}_2} (\hat{c}_{e, \vec{n}_1}^\dagger \hat{c}_{g, \vec{n}_2}^\dagger \hat{c}_{g, \vec{n}_1} \hat{c}_{e, \vec{n}_2} + \hat{c}_{e, \vec{n}_1}^\dagger \hat{c}_{g, \vec{n}_2}^\dagger \hat{c}_{g, \vec{n}_2} \hat{c}_{e, \vec{n}_1} + \hat{c}_{g, \vec{n}_1}^\dagger \hat{c}_{e, \vec{n}_2}^\dagger \hat{c}_{e, \vec{n}_1} \hat{c}_{g, \vec{n}_2} + \hat{c}_{g, \vec{n}_1}^\dagger \hat{c}_{e, \vec{n}_2}^\dagger \hat{c}_{e, \vec{n}_2} \hat{c}_{g, \vec{n}_1}) \\ &= \frac{2\pi\hbar}{m} R_r^2 R_z a_{eg}^- \sum_{\vec{n}_1 \neq \vec{n}_2} S_{\vec{n}_1, \vec{n}_2} (-\hat{c}_{e, \vec{n}_1}^\dagger \hat{c}_{g, \vec{n}_1} \hat{c}_{g, \vec{n}_2}^\dagger \hat{c}_{e, \vec{n}_2} + \hat{c}_{e, \vec{n}_1}^\dagger \hat{c}_{e, \vec{n}_1} \hat{c}_{g, \vec{n}_2}^\dagger \hat{c}_{g, \vec{n}_2} - \hat{c}_{g, \vec{n}_1}^\dagger \hat{c}_{e, \vec{n}_1} \hat{c}_{e, \vec{n}_2}^\dagger \hat{c}_{g, \vec{n}_2} + \hat{c}_{g, \vec{n}_1}^\dagger \hat{c}_{g, \vec{n}_1} \hat{c}_{e, \vec{n}_2}^\dagger \hat{c}_{e, \vec{n}_2}). \end{aligned}$$

Next we do the following mapping:

$$\begin{aligned} \frac{1}{2}(\hat{c}_{e, \vec{n}_i}^\dagger \hat{c}_{e, \vec{n}_i} - \hat{c}_{g, \vec{n}_i}^\dagger \hat{c}_{g, \vec{n}_i}) &= \hat{S}_{n_i}^z, & \frac{1}{2}(\hat{c}_{e, \vec{n}_i}^\dagger \hat{c}_{g, \vec{n}_i} + \hat{c}_{g, \vec{n}_i}^\dagger \hat{c}_{e, \vec{n}_i}) &= \hat{S}_{n_i}^x, \\ \frac{i}{2}(\hat{c}_{g, \vec{n}_i}^\dagger \hat{c}_{e, \vec{n}_i} - \hat{c}_{e, \vec{n}_i}^\dagger \hat{c}_{g, \vec{n}_i}) &= \hat{S}_{n_i}^y, & \hat{c}_{e, \vec{n}_i}^\dagger \hat{c}_{e, \vec{n}_i} + \hat{c}_{g, \vec{n}_i}^\dagger \hat{c}_{g, \vec{n}_i} &= \hat{I}_{n_i}. \end{aligned} \quad (\text{A2})$$

Then \hat{H}_0^s becomes

$$\hat{H}_0^s = -\frac{4\pi\hbar^2}{m} R_r^2 R_z a_{eg}^- \sum_{\vec{n}_1 \neq \vec{n}_2} S_{\vec{n}_1, \vec{n}_2} \hat{S}_{n_1} \cdot \hat{S}_{n_2}.$$

Now we turn to the p -wave scattering Hamiltonian \hat{H}_0^p . After expanding the field operator under the Harmonic eigenbasis, we have

$$\begin{aligned} \hat{H}_0^p &= \frac{3\pi\hbar^2}{m} \sum_{\alpha, \beta} b_{\alpha\beta}^3 \sum_{\vec{n}_1, \vec{n}_2, \vec{n}_3, \vec{n}_4} \hat{c}_{\alpha, \vec{n}_1}^\dagger \hat{c}_{\beta, \vec{n}_2}^\dagger \hat{c}_{\beta, \vec{n}_3} \hat{c}_{\alpha, \vec{n}_4} \left[\int \left(\frac{\partial \phi_{n_{x_1}}}{\partial \xi_x} \phi_{n_2} - \phi_{n_{x_1}} \frac{\partial \phi_{n_{x_2}}}{\partial \xi_x} \right) \left(\phi_{n_{x_3}} \frac{\partial \phi_{n_{x_4}}}{\partial \xi_x} - \frac{\partial \phi_{n_{x_3}}}{\partial \xi_x} \phi_{n_4} \right) dx \right. \\ &\quad \times R_r^3 R_z s(n_{y_1}, n_{y_2}, n_{y_3}, n_{y_4}) s(n_{z_1}, n_{z_2}, n_{z_3}, n_{z_4}) + \int \left(\frac{\partial \phi_{n_{y_1}}}{\partial \xi_y} \phi_{n_2} - \phi_{n_{y_1}} \frac{\partial \phi_{n_{y_2}}}{\partial \xi_y} \right) \left(\phi_{n_{y_3}} \frac{\partial \phi_{n_{y_4}}}{\partial \xi_y} - \frac{\partial \phi_{n_{y_3}}}{\partial \xi_y} \phi_{n_4} \right) dy \\ &\quad \times R_r^3 R_z s(n_{x_1}, n_{x_2}, n_{x_3}, n_{x_4}) s(n_{z_1}, n_{z_2}, n_{z_3}, n_{z_4}) + \int \left(\frac{\partial \phi_{n_{z_1}}}{\partial \xi_z} \phi_{n_2} - \phi_{n_{z_1}} \frac{\partial \phi_{n_{z_2}}}{\partial \xi_z} \right) \left(\phi_{n_{z_3}} \frac{\partial \phi_{n_{z_4}}}{\partial \xi_z} - \frac{\partial \phi_{n_{z_3}}}{\partial \xi_z} \phi_{n_4} \right) dz \\ &\quad \left. \times R_z^2 R_r^2 s(n_{x_1}, n_{x_2}, n_{x_3}, n_{x_4}) s(n_{y_1}, n_{y_2}, n_{y_3}, n_{y_4}) \right]. \end{aligned}$$

By defining

$$p(n_1, n_2, n_3, n_4) = \int \frac{\left(\frac{dH_{n_1}}{d\xi} H_{n_2} - H_{n_1} \frac{dH_{n_2}}{d\xi} \right) \left(\frac{dH_{n_3}}{d\xi} H_{n_4} - H_{n_3} \frac{dH_{n_4}}{d\xi} \right)}{\pi \sqrt{2^{n_1+n_2+n_3+n_4} n_1! n_2! n_3! n_4!}} e^{-2\xi^2} d\xi,$$

where the mode dependence of $p(n_1, n_2, n_1, n_2)$ is shown in Fig. 16, and considering the collision rule (A1), \hat{H}_0^p could be written as

$$\begin{aligned} \hat{H}_0^p &= -\frac{3\pi\hbar^2}{m} \sum_{\alpha, \beta} b_{\alpha\beta}^3 \sum_{\vec{n}_1 \neq \vec{n}_2} \hat{c}_{\alpha, \vec{n}_1}^\dagger \hat{c}_{\beta, \vec{n}_2}^\dagger \hat{c}_{\beta, \vec{n}_1} \hat{c}_{\alpha, \vec{n}_2} \left[R_r^4 R_z p(n_{x_1}, n_{x_2}, n_{x_1}, n_{x_2}) s(n_{y_1}, n_{y_2}, n_{y_1}, n_{y_2}) s(n_{z_1}, n_{z_2}, n_{z_1}, n_{z_2}) \right. \\ &\quad + R_r^4 R_z p(n_{y_1}, n_{y_2}, n_{y_1}, n_{y_2}) s(n_{x_1}, n_{x_2}, n_{x_1}, n_{x_2}) s(n_{z_1}, n_{z_2}, n_{z_1}, n_{z_2}) \\ &\quad + R_z^3 R_r^2 p(n_{z_1}, n_{z_2}, n_{z_1}, n_{z_2}) s(n_{x_1}, n_{x_2}, n_{x_1}, n_{x_2}) s(n_{y_1}, n_{y_2}, n_{y_1}, n_{y_2}) \left. \right] \\ &\quad + \hat{c}_{\alpha, \vec{n}_1}^\dagger \hat{c}_{\beta, \vec{n}_2}^\dagger \hat{c}_{\beta, \vec{n}_2} \hat{c}_{\alpha, \vec{n}_1} \left[R_r^4 R_z p(n_{x_1}, n_{x_2}, n_{x_2}, n_{x_1}) s(n_{y_1}, n_{y_2}, n_{y_2}, n_{y_1}) s(n_{z_1}, n_{z_2}, n_{z_2}, n_{z_1}) + R_r^4 R_z p(n_{y_1}, n_{y_2}, n_{y_2}, n_{y_1}) \right. \\ &\quad \times s(n_{x_1}, n_{x_2}, n_{x_2}, n_{x_1}) s(n_{z_1}, n_{z_2}, n_{z_2}, n_{z_1}) + R_z^3 R_r^2 p(n_{z_1}, n_{z_2}, n_{z_2}, n_{z_1}) s(n_{x_1}, n_{x_2}, n_{x_2}, n_{x_1}) s(n_{y_1}, n_{y_2}, n_{y_2}, n_{y_1}) \left. \right]. \end{aligned}$$

By defining

$$\begin{aligned} P_{\vec{n}_i, \vec{n}_j}^r &= p(n_{x_i}, n_{x_j}, n_{x_j}, n_{x_i}) s(n_{y_i}, n_{y_j}, n_{y_j}, n_{y_i}) s(n_{z_i}, n_{z_j}, n_{z_j}, n_{z_i}) + p(n_{y_i}, n_{y_j}, n_{y_j}, n_{y_i}) s(n_{x_i}, n_{x_j}, n_{x_j}, n_{x_i}) s(n_{z_i}, n_{z_j}, n_{z_j}, n_{z_i}), \\ P_{\vec{n}_i, \vec{n}_j}^z &= p(n_{z_i}, n_{z_j}, n_{z_j}, n_{z_i}) s(n_{x_i}, n_{x_j}, n_{x_j}, n_{x_i}) s(n_{y_i}, n_{y_j}, n_{y_j}, n_{y_i}) \end{aligned}$$

and noting that $p(n_1, n_2, n_2, n_1) = -p(n_1, n_2, n_1, n_2)$, we have

$$\hat{H}_0^p = -\frac{3\pi\hbar^2}{m} \sum_{\alpha,\beta} b_{\alpha\beta}^3 \sum_{\vec{n}_1 \neq \vec{n}_2} (R_r^4 R_z P_{\vec{n}_1, \vec{n}_2}^r + R_r^2 R_z^3 P_{\vec{n}_1, \vec{n}_2}^z) (\hat{c}_{\alpha, \vec{n}_1}^\dagger \hat{c}_{\beta, \vec{n}_2}^\dagger \hat{c}_{\beta, \vec{n}_2} \hat{c}_{\alpha, \vec{n}_1} - \hat{c}_{\alpha, \vec{n}_1}^\dagger \hat{c}_{\beta, \vec{n}_2}^\dagger \hat{c}_{\beta, \vec{n}_1} \hat{c}_{\alpha, \vec{n}_2}).$$

After mapping (A2), we get the spin Hamiltonian for p -wave scattering,

$$\hat{H}_0^p = -\frac{3\pi\hbar^2}{m} \sum_{\vec{n}_1 \neq \vec{n}_2} (R_r^4 R_z P_{\vec{n}_1, \vec{n}_2}^r + R_r^2 R_z^3 P_{\vec{n}_1, \vec{n}_2}^z) [S_{\vec{n}_1}^z S_{\vec{n}_2}^z (2b_{ee}^3 - 4b_{eg}^3 + 2b_{gg}^3) + \hat{S}_{\vec{n}_1} \cdot \hat{S}_{\vec{n}_2} 2b_{eg}^3 + (I_{\vec{n}_1} S_{\vec{n}_2}^z + S_{\vec{n}_1}^z I_{\vec{n}_2}) (b_{ee}^3 - b_{gg}^3)].$$

Finally, let us turn to the Rabi term \hat{H}_0^{Rabi} . After expanding, we have

$$\begin{aligned} \hat{H}_0^{\text{Rabi}} &= \frac{1}{2} \hbar \omega_0 \sum_{\vec{n}} \hat{c}_{e, \vec{n}}^\dagger \hat{c}_{e, \vec{n}} - \hat{c}_{g, \vec{n}}^\dagger \hat{c}_{g, \vec{n}} - \hbar \pi \Omega_0 \left(e^{-i\omega_L t} \sum_{\vec{n}_1, \vec{n}_2} \int \phi_{\vec{n}_1}(\mathbf{r}) e^{i\mathbf{k} \cdot \mathbf{r}} \phi_{\vec{n}_2}(\mathbf{r}) d\mathbf{r} \hat{c}_{e, \vec{n}_1}^\dagger \hat{c}_{g, \vec{n}_2} \right) \\ &\quad - \hbar \pi \Omega_0 \left(e^{i\omega_L t} \sum_{\vec{n}_1, \vec{n}_2} \int \phi_{\vec{n}_1}(\mathbf{r}) e^{-i\mathbf{k} \cdot \mathbf{r}} \phi_{\vec{n}_2}(\mathbf{r}) d\mathbf{r} \hat{c}_{e, \vec{n}_1}^\dagger \hat{c}_{g, \vec{n}_2} \right). \end{aligned}$$

During the experiment, a small misalignment angle θ ($\theta \approx 5$ mrad) exists between the radial and longitude directions. Therefore, the wave vector of the probing light could be

$$\mathbf{k} = k_L(\sin\theta, 0, \cos\theta) \approx k_L(\theta, 0, 1).$$

By defining

$$\begin{aligned} \Omega_{\vec{n}} &= \Omega_0 \int \phi_{\vec{n}_1}(\mathbf{r}) e^{i\mathbf{k} \cdot \mathbf{r}} \phi_{\vec{n}_2}(\mathbf{r}) d\mathbf{r} \\ &= \Omega_0 e^{-\frac{1}{2}(\eta_z^2 + \eta_x^2)} L_{n_x}(\eta_x^2) L_{n_z}(\eta_z^2), \end{aligned}$$

where $\eta_x = \sqrt{\frac{\hbar}{2m\omega_r}} \frac{\theta}{\lambda_p}$ and $\eta_z = \sqrt{\frac{\hbar}{2m\omega_z}} \frac{1}{\lambda_p}$ are the Lamb-Dicke parameters in the x and z directions, respectively (with $\lambda_p = 698$ nm the wavelength of the probing laser), and L_n is the Laguerre polynomial, \hat{H}_0^{Rabi} can be simplified as

$$\begin{aligned} \hat{H}_0^{\text{Rabi}} &= \frac{1}{2} \hbar \omega_0 \sum_{\vec{n}} \hat{c}_{e, \vec{n}}^\dagger \hat{c}_{e, \vec{n}} - \hat{c}_{g, \vec{n}}^\dagger \hat{c}_{g, \vec{n}} - \hbar \pi \sum_{\vec{n}} \Omega_{\vec{n}} (e^{-i\omega_L t} \hat{c}_{e, \vec{n}}^\dagger \hat{c}_{g, \vec{n}} + e^{i\omega_L t} \hat{c}_{g, \vec{n}}^\dagger \hat{c}_{e, \vec{n}}) \\ &= \hbar \omega_0 \sum_{\vec{n}} \hat{S}_{\vec{n}}^z - \hbar \pi \sum_{\vec{n}} \Omega_{\vec{n}} (e^{-i\omega_L t} \hat{S}_{\vec{n}}^+ + e^{i\omega_L t} \hat{S}_{\vec{n}}^-). \end{aligned}$$

Thus \hat{H}_0 becomes

$$\begin{aligned} \hat{H}_0 &= -\frac{4\pi\hbar^2}{m} R_r^2 R_z a_{eg}^- \sum_{\vec{n}_1 \neq \vec{n}_2} S_{\vec{n}_1, \vec{n}_2} \hat{S}_{n_1} \cdot \hat{S}_{n_2} - \frac{3\pi\hbar^2}{m} \sum_{\vec{n}_1 \neq \vec{n}_2} (R_r^4 R_z P_{\vec{n}_1, \vec{n}_2}^r + R_r^2 R_z^3 P_{\vec{n}_1, \vec{n}_2}^z) [S_{\vec{n}_1}^z S_{\vec{n}_2}^z (2b_{ee}^3 - 4b_{eg}^3 + 2b_{gg}^3) + \hat{S}_{\vec{n}_1} \cdot \hat{S}_{\vec{n}_2} 2b_{eg}^3 \\ &\quad + (\hat{I}_{\vec{n}_1} \hat{S}_{\vec{n}_2}^z + \hat{S}_{\vec{n}_1}^z \hat{I}_{\vec{n}_2}) (b_{ee}^3 - b_{gg}^3)] + \hbar \omega_0 \sum_{\vec{n}} \hat{S}_{\vec{n}}^z - \hbar \pi \sum_{\vec{n}} \Omega_{\vec{n}} (e^{-i\omega_L t} \hat{S}_{\vec{n}}^+ + e^{i\omega_L t} \hat{S}_{\vec{n}}^-). \end{aligned}$$

Next we apply a rotation frame transformation $\hat{U} = \exp(i\omega_L t \sum_{\vec{n}} \hat{S}_{\vec{n}}^z)$. After the transformation, we will get the effective spin Hamiltonian in the rotated frame $\hat{H}_s = \hat{U}(\hat{H}_0 - i\hbar \frac{\partial}{\partial t})\hat{U}^\dagger$. Note that $[\hat{U}, \hat{H}_0^p] = [\hat{U}, \hat{H}_0^s] = 0$; therefore, we should only pay attention to $\hat{U} \sum_{\vec{n}} \Omega_{\vec{n}} (e^{-i\omega_L t} \hat{S}_{\vec{n}}^+ + e^{i\omega_L t} \hat{S}_{\vec{n}}^-) \hat{U}^\dagger$:

$$\begin{aligned} \hat{U} \left(\sum_{\vec{n}} \Omega_{\vec{n}} e^{-i\omega_L t} \hat{S}_{\vec{n}}^+ + e^{i\omega_L t} \hat{S}_{\vec{n}}^- \right) \hat{U}^\dagger &= \sum_{\vec{n}_1, \vec{n}_2, \vec{n}_3} e^{-i\omega_L t \sum_{\vec{n}_1} \hat{S}_{\vec{n}_1}^z} \Omega_{\vec{n}_2} (e^{-i\omega_L t} \hat{S}_{\vec{n}_2}^+ + e^{i\omega_L t} \hat{S}_{\vec{n}_2}^-) e^{i\omega_L t \sum_{\vec{n}_3} \hat{S}_{\vec{n}_3}^z} \\ &= \sum_{\vec{n}} \Omega_{\vec{n}} e^{i\omega_L t \hat{S}_{\vec{n}}^z} (e^{-i\omega_L t} \hat{S}_{\vec{n}}^+ + e^{i\omega_L t} \hat{S}_{\vec{n}}^-) e^{-i\omega_L t \hat{S}_{\vec{n}}^z} \\ &= \sum_{\vec{n}} 2\Omega_{\vec{n}} \hat{S}_{\vec{n}}^x. \end{aligned}$$

Therefore,

$$\begin{aligned} \hat{H}_s = & -\frac{4\pi\hbar^2}{m} R_r^2 R_z a_{eg}^- \sum_{\vec{n}_1 \neq \vec{n}_2} S_{\vec{n}_1, \vec{n}_2} \hat{S}_{\vec{n}_1} \cdot \hat{S}_{\vec{n}_2} - \frac{3\pi\hbar^2}{m} \sum_{\vec{n}_1 \neq \vec{n}_2} (R_r^4 R_z P_{\vec{n}_1, \vec{n}_2}^r + R_r^2 R_z^3 P_{\vec{n}_1, \vec{n}_2}^z) [S_{\vec{n}_1}^z S_{\vec{n}_2}^z (2b_{ee}^3 - 4b_{eg}^3 + 2b_{gg}^3) + \hat{S}_{\vec{n}_1} \cdot \hat{S}_{\vec{n}_2} 2b_{eg}^3 \\ & + (\hat{I}_{\vec{n}_1} \hat{S}_{\vec{n}_2}^z + \hat{S}_{\vec{n}_1}^z \hat{I}_{\vec{n}_2}) (b_{ee}^3 - b_{gg}^3)] + \hbar(\omega_0 - \omega_L) \sum_{\vec{n}} \hat{S}_{\vec{n}}^z - \hbar \sum_{\vec{n}} 2\pi \Omega_{\vec{n}} \hat{S}_{\vec{n}}^x. \end{aligned}$$

By defining

$$\begin{aligned} G_{i,j}^S &= \frac{4\pi\hbar}{m} R_r^2 R_z S_{\vec{n}_1, \vec{n}_2}, \\ G_{i,j}^P &= \frac{6\pi\hbar}{m} (R_r^4 R_z P_{\vec{n}_1, \vec{n}_2}^r + R_r^2 R_z^3 P_{\vec{n}_1, \vec{n}_2}^z) \end{aligned}$$

and using the definition in (4), we finally obtain the effective spin Hamiltonian (3),

$$\frac{\hat{H}}{\hbar} = -2\pi\delta \sum_i \hat{S}_i^z - 2\pi \sum_i \Omega_i \hat{S}_i^x - \sum_{i \neq j} C_{i,j} \frac{\hat{S}_i^z + \hat{S}_j^z}{2} - \sum_{i \neq j} X_{i,j} \hat{S}_i^z \hat{S}_j^z - \sum_{i \neq j} J_{i,j} \vec{S}_i \cdot \vec{S}_j,$$

with $\delta = \frac{\omega_L - \omega_0}{2\pi}$.

APPENDIX B: COLLECTIVE APPROXIMATION

The interaction strengths $G_{i,j}^S$ and $G_{i,j}^P$ and Rabi frequency Ω_i are related to the motional degree of freedom. However, their standard deviations ($\Delta G_{i,j}^S$, $\Delta G_{i,j}^P$, and $\Delta \Omega_i$) are very small in a collective regime, which requires the temperature to be low and the misaligned angle to be tiny. Therefore, the collective approximation can be utilized and it stands that these mode-dependent parameters can be replaced with their average value. Then the Hamiltonian (3) can be approximately written as

$$\hat{H}_{\text{col}}/\hbar = -2\pi\delta \hat{S}^z - 2\pi \bar{\Omega} \hat{S}^x - \bar{X} \hat{S}^z \hat{S}^z - (N-1) \bar{C} \hat{S}^z,$$

where

$$\begin{aligned} \hat{S}^{\gamma=x,y,z} &= \sum_i \hat{S}_i^{\gamma}, \quad \bar{\Omega} = \frac{\sum_i \Omega_i}{N}, \\ \bar{X} &= \frac{\sum_{i \neq j} X_{i,j}}{N(N-1)}, \quad \bar{C} = \frac{\sum_{i \neq j} C_{i,j}}{N(N-1)}. \end{aligned}$$

Under the collective approximation, the quantum state is restricted in the subspace of the Hilbert space with total spin $S = \frac{N}{2}$. Therefore, the Heisenberg term in the Hamiltonian (3) is a constant and can be ignored.

APPENDIX C: FITTING THE SCATTERING LENGTH

The experiment we considered is that in Ref. [23] by Martin *et al.*, so the parameters are set to $\Delta\theta = 5$ mrad, $\nu_r = 450$ Hz, $\nu_z = 80$ kHz, $T_r = 3$ μ K, and $T_z = 1.5$ μ K. In the experiment [23], the average number of atoms in each site was about 20, which is still large for our method. Thus, we set the atom number to 12 and obtain the density shift of 20 atoms after rescaling due to the linear relation in high density. Considering the low temperature and small misaligned angle $\Delta\theta$, the truncation of Hilbert space could be used. As demonstrated in Fig. 17, only two subspaces need to be taken into account.

After calculating the density shift of 12 atoms, we can obtain the density shift of 20 atoms by multiplying by a factor of $\frac{19}{11}$. As shown in Fig. 18, the experimental data and the fitting data match well, while the fitted scattering lengths are $b_{eg} = 192.34a_B$ and $b_{ee} = 150.19a_B$.

APPENDIX D: DENSITY SHIFT UNDER THE COLLECTIVE APPROXIMATION

The density shift in the Ramsey spectroscopy could be analytically calculated approximately. According to Sec. IV, the time-evolution operator in the Ramsey process could be written as

$$\hat{U}(t_1, \tau, t_2) = e^{-it_2 \hat{H}_p/\hbar} e^{-i\tau \hat{H}_d/\hbar} e^{-it_1 \hat{H}_p/\hbar},$$

where the Hamiltonian during the pulse time is

$$\hat{H}_p/\hbar = -2\pi \bar{\Omega} \hat{S}^x$$

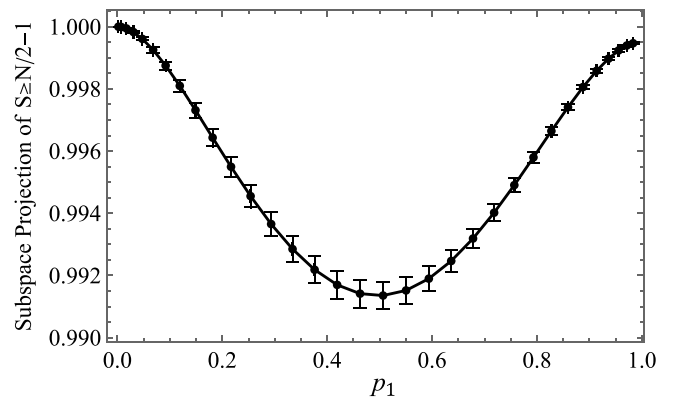


FIG. 17. Numerical results of projection in the subspace with total spin equal to $S = \frac{N}{2}$ and $\frac{N}{2} - 1$ for different excitation fractions at the end of the dark time in the Ramsey spectroscopy. The number of atoms is 12 and the other parameters are the same as in the experiment in [23].

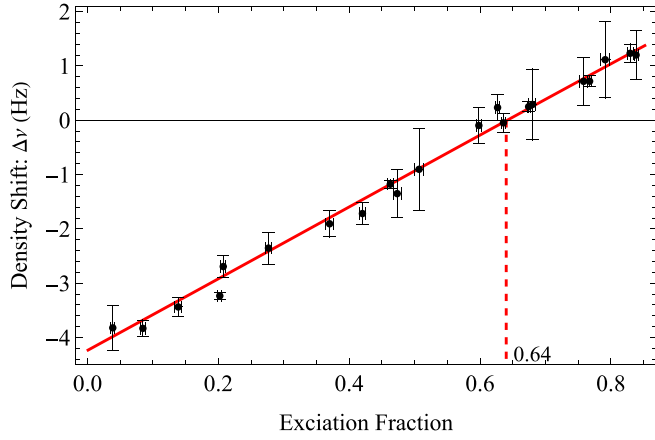


FIG. 18. Experimental results in Ref. [23] (black circles) and the fitting numerical results (red solid line) of the density shift for different excitation fractions. The fitted scattering lengths are $b_{eg} = 192.34a_B$ and $b_{ee} = 150.19a_B$.

and the Hamiltonian during the dark time can be expressed as

$$\hat{H}_d/\hbar = -2\pi\delta\hat{S}^z - \bar{X}\hat{S}^z\hat{S}^z - (N-1)\bar{C}\hat{S}^z.$$

Here, approximately \hat{H}_p does not consider atomic collision and detuning and \hat{H}_d does not consider the atom-light interaction. We use $|t_1, \tau, t_2\rangle = \hat{U}(t_1, \tau, t_2)|0\rangle$ to define the quantum state during the Ramsey process, and the measurement at the end of the dark time should be

$$\langle\hat{S}^z\rangle_{t_1, \tau, 0} = -\frac{N}{2} \cos(2\pi\bar{\Omega}t_1),$$

$$\langle\hat{S}^x\rangle_{t_1, \tau, 0} = -\frac{N}{2} \sin(2\pi\bar{\Omega}t_1) \sin\{[2\pi\delta + (N-1)(\bar{C} - \ell)]\tau\} \times Z^{N-1},$$

$$\langle\hat{S}^y\rangle_{t_1, \tau, 0} = -\frac{N}{2} \sin(2\pi\bar{\Omega}t_1) \cos\{[2\pi\delta + (N-1)(\bar{C} - \ell)]\tau\} \times Z^{N-1},$$

with

$$Z = \sqrt{\cos^2 \bar{X}\tau + \cos^2 2\pi\bar{\Omega}t_1 \sin^2 \bar{X}\tau},$$

$$\tan \ell\tau = \cos 2\pi\bar{\Omega}t_1 \tan \bar{X}\tau.$$

If $\bar{X}\tau \ll 1$, then the density shift is

$$2\pi\Delta\nu = (N-1)(\ell - \bar{C}) \approx (N-1)(\bar{X} \cos 2\pi\bar{\Omega}t_1 - \bar{C}).$$

-
- [1] S. Blatt, A. D. Ludlow, G. K. Campbell, J. W. Thomsen, T. Zelevinsky, M. M. Boyd, J. Ye, X. Baillard, M. Fouché, R. Le Targat, A. Brusch, P. Lemonde, M. Takamoto, F.-L. Hong, H. Katori, and V. V. Flambaum, *Phys. Rev. Lett.* **100**, 140801 (2008).
 - [2] S. Kolkowitz, I. Pikovski, N. Langellier, M. D. Lukin, R. L. Walsworth, and J. Ye, *Phys. Rev. D* **94**, 124043 (2016).
 - [3] M. Takamoto, I. Ushijima, N. Ohmae, T. Yahagi, K. Kokado, H. Shinkai, and H. Katori, *Nat. Photon.* **14**, 411 (2020).
 - [4] T. Bothwell, C. J. Kennedy, A. Aeppli, D. Kedar, J. M. Robinson, E. Oelker, A. Staron, and J. Ye, *Nature (London)* **602**, 420 (2022).
 - [5] X. Zheng, J. Dolde, V. Lochab, B. N. Merriman, H. Li, and S. Kolkowitz, *Nature (London)* **602**, 425 (2022).
 - [6] A. Derevianko and M. Pospelov, *Nat. Phys.* **10**, 933 (2014).
 - [7] A. Arvanitaki, J. Huang, and K. Van Tilburg, *Phys. Rev. D* **91**, 015015 (2015).
 - [8] M. Takamoto, T. Takano, and H. Katori, *Nat. Photon.* **5**, 288 (2011).
 - [9] A. D. Ludlow, T. Zelevinsky, G. K. Campbell, S. Blatt, M. M. Boyd, M. H. G. de Miranda, M. J. Martin, J. W. Thomsen, S. M. Foreman, J. Ye, T. M. Fortier, J. E. Stalnaker, S. A. Diddams, Y. Le Coq, Z. W. Barber, N. Poli, N. D. Lemke, K. M. Beck, and C. W. Oates, *Science* **319**, 1805 (2008).
 - [10] A. V. Gorshkov, M. Hermele, V. Gurarie, C. Xu, P. S. Julienne, J. Ye, P. Zoller, E. Demler, M. D. Lukin, and A. M. Rey, *Nat. Phys.* **6**, 289 (2010).
 - [11] M. Foss-Feig, M. Hermele, and A. M. Rey, *Phys. Rev. A* **81**, 051603(R) (2010).
 - [12] M. Foss-Feig, M. Hermele, V. Gurarie, and A. M. Rey, *Phys. Rev. A* **82**, 053624 (2010).
 - [13] M. A. Cazalilla, A. F. Ho, and M. Ueda, *New J. Phys.* **11**, 103033 (2009).
 - [14] X. Zhang, M. Bishof, S. L. Bromley, C. V. Kraus, M. S. Safronova, P. Zoller, A. M. Rey, and J. Ye, *Science* **345**, 1467 (2014).
 - [15] G. Chen and C. Wu, *arXiv:2112.02630*.
 - [16] M. Mamaev, I. Kimchi, R. M. Nandkishore, and A. M. Rey, *Phys. Rev. Res.* **3**, 013178 (2021).
 - [17] A. Aeppli, A. Chu, T. Bothwell, C. J. Kennedy, D. Kedar, P. He, A. M. Rey, and J. Ye, *Sci. Adv.* **8**, eadc9242 (2022).
 - [18] A. V. Gorshkov, A. M. Rey, A. J. Daley, M. M. Boyd, J. Ye, P. Zoller, and M. D. Lukin, *Phys. Rev. Lett.* **102**, 110503 (2009).
 - [19] A. J. Daley, M. M. Boyd, J. Ye, and P. Zoller, *Phys. Rev. Lett.* **101**, 170504 (2008).
 - [20] D. Hayes, P. S. Julienne, and I. H. Deutsch, *Phys. Rev. Lett.* **98**, 070501 (2007).
 - [21] S. Blatt, J. W. Thomsen, G. K. Campbell, A. D. Ludlow, M. D. Swallows, M. J. Martin, M. M. Boyd, and J. Ye, *Phys. Rev. A* **80**, 052703 (2009).
 - [22] A. Rey, A. Gorshkov, C. Kraus, M. Martin, M. Bishof, M. Swallows, X. Zhang, C. Benko, J. Ye, N. Lemke, and A. Ludlow, *Ann. Phys. (NY)* **340**, 311 (2014).
 - [23] M. J. Martin, M. Bishof, M. D. Swallows, X. Zhang, C. Benko, J. von Stecher, A. V. Gorshkov, A. M. Rey, and J. Ye, *Science* **341**, 632 (2013).
 - [24] S. B. Koller, J. Grotti, S. Vogt, A. Al-Masoudi, S. Dörscher, S. Häfner, U. Sterr, and C. Lisdat, *Phys. Rev. Lett.* **118**, 073601 (2017).
 - [25] S. Origlia, M. S. Pramod, S. Schiller, Y. Singh, K. Bongs, R. Schwarz, A. Al-Masoudi, S. Dörscher, S. Herbers, S. Häfner, U. Sterr, and C. Lisdat, *Phys. Rev. A* **98**, 053443 (2018).
 - [26] J. Ye, H. J. Kimble, and H. Katori, *Science* **320**, 1734 (2008).

- [27] A. M. Rey, A. V. Gorshkov, and C. Rubbo, [Phys. Rev. Lett. **103**, 260402 \(2009\)](#).
- [28] Z. Yu and C. J. Pethick, [Phys. Rev. Lett. **104**, 010801 \(2010\)](#).
- [29] K. R. A. Hazzard, A. V. Gorshkov, and A. M. Rey, [Phys. Rev. A **84**, 033608 \(2011\)](#).
- [30] M. Bishof, M. J. Martin, M. D. Swallows, C. Benko, Y. Lin, G. Quémener, A. M. Rey, and J. Ye, [Phys. Rev. A **84**, 052716 \(2011\)](#).
- [31] A. W. Young, W. J. Eckner, W. R. Milner, D. Kedar, M. A. Norcia, E. Oelker, N. Schine, J. Ye, and A. M. Kaufman, [Nature \(London\) **588**, 408 \(2020\)](#).